Journal of Colloid and Interface Science 592 (2021) 485–497

Contents lists available at ScienceDirect

Journal of Colloid and Interface Science

journal homepage: www.elsevier.com/locate/jcis

Regular Article

Metformin derived carbon dots: Highly biocompatible fluorescent nanomaterials as mitochondrial targeting and blood-brain barrier penetrating biomarkers

Emel Kirbas Cilingir [a], Elif S. Seven [a], Yiqun Zhou [a], Brian M. Walters [b], Keenan J. Mintz [a], Raja R. Pandey [c], Athula H. Wikramanayake [b], Charles C. Chusuei [c], Steven Vanni [d], Regina M. Graham [d], Roger M. Leblanc [a,*]

[a] Department of Chemistry, University of Miami, 1301 Memorial Drive, Coral Gables, FL 33146, United States
[b] Department of Biology, University of Miami, Coral Gables, FL 33146, United States
[c] Department of Chemistry, Middle Tennessee State University, Murfreesboro, TN 37132, United States
[d] Department of Neurological Surgery, Miller School of Medicine, University of Miami, Miami, FL 33136, United States

HIGHLIGHTS

- Metformin was used as a precursor to synthesize carbon dots, for the first time.
- Met-CDs showed excellent biocompatibility towards both non-tumor and tumor cells.
- Met-CDs can penetrate the cell membrane and disperse throughout the cell including the nucleus and mitochondria.
- After 1 hour of treatment, Met-CDs tend to localize inside the mitochondria.
- Met-CDs can cross the blood–brain barrier without the need of any other ligand on their surface.

GRAPHICAL ABSTRACT

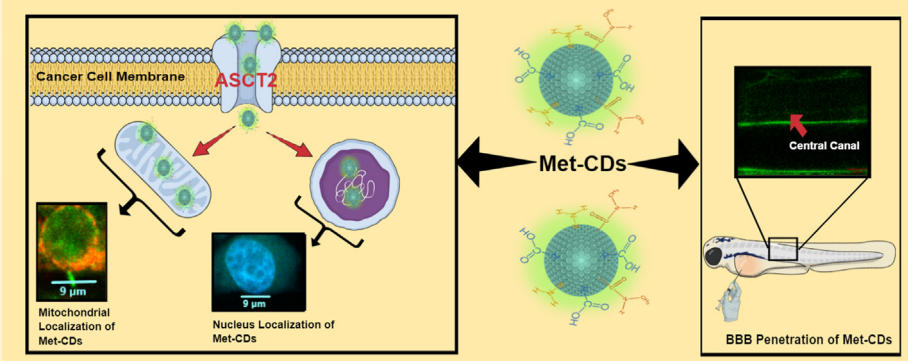

ARTICLE INFO

Article history:
Received 28 November 2020
Revised 11 February 2021
Accepted 12 February 2021
Available online 19 February 2021

Keywords:
Met-CDs
Biomarker
Bioimaging
Mitochondrial and nucleus targeting
BBB penetration

ABSTRACT

Carbon dots (CDs) have been intensively studied since their discovery in 2004 because of their unique properties such as low toxicity, excellent biocompatibility, high photoluminescence (PL) and good water dispersibility. In this study metformin derived carbon dots (Met-CDs) were synthesized using a microwave assisted method. Met-CDs were meticulously characterized using ultra-violet spectroscopy (UV–vis), photoluminescence (PL), Fourier Transform Infrared spectroscopy (FTIR), X-ray photoelectron spectroscopy (XPS), atomic force (AFM) and transmission electron (TEM) microscopies. According to results of cytotoxicity studies, Met-CDs possess low-toxicity and excellent biocompatibility towards both non-tumor and tumor cell lines indicating that Met-CDs are outstanding candidates for living cell bioimaging studies. Furthermore, bioimaging studies have displayed that Met-CDs can penetrate the cell membrane and disperse throughout the cell structure including the nucleus and mitochondria. More specifically, Met-CDs tend to start localizing selectively inside the mitochondria of cancer cells, but not of non-tumor cells after 1 h of incubation. Finally, a zebrafish study confirmed that Met-CDs cross the blood–brain barrier (BBB) without the need of any other ligands. In summary, this study presents synthesis of Met-CDs which feature abilities such as mitochondrial and nucleus localizations along with BBB penetration.

* Corresponding author at: University of Miami, Dept. Chemistry, 1301 Memorial Drive, Coral Gables, FL 33146, USA.
E-mail address: rml@miami.edu (R.M. Leblanc).

https://doi.org/10.1016/j.jcis.2021.02.058
0021-9797/

1. Introduction

Carbon dots (CDs) have called enormous attention from the scientific community thanks to their exceptional photoluminescence (PL), high photo stability, excellent biocompatibility and remarkable tunable surface functionality, which favor a huge potential for biomedical applications [1]. Compared to the traditional semiconductor quantum dots, CDs are nontoxic and environment friendly. Consequently, all these unique characteristics have triggered rapid development of carbon dots as nanomaterials [2,3]. CDs are classified as zero-dimensional nanocarbons, or carbon nanoparticles, which have less than 10 nm size across with a crystal lattice parameter of 0.34 nm corresponding to the (0 0 2) interlayer spacing of graphite [4,5,6]. There are two well accepted approaches for the synthesis of CDs: bottom-up and top-down. The bottom-up approach involves ionization, polymerization, and carbonization (pyrolysis) of small organic molecules or stepwise chemical fusion of small aromatic molecules. Alternatively, the top-down approach is related to breaking down larger carbon structures to smaller units by using chemical, electrochemical, or physical methods such as acid reflux, electrolysis, and laser ablation [1]. More importantly, researchers have been using a variety of organic precursors from fruit juice to carbon ash to synthesize CDs with different properties depending on intended research purposes [7,8]. Directly, presence of abundant choices of precursors provides exclusive advantages such as ease of preparation and lower cost. Some studies use small molecules as precursors for CDs, with the expectation that some of the precursor structure will remain on the surface of CDs and so incorporate the capability of the original molecule to the precursor product. This study uses metformin for this purpose [9] (see Scheme 1).

Metformin is a widely prescribed drug for the treatment of type 2 diabetes mellitus [10]. It is a biguanide (containing two linked guanidine rings) refined from galegine, a guanidine derivative found in *Galega officinalis* (French lilac) [11]. During the middle ages, *Galega officinalis* was used to relieve intense urination, a symptom that accompanies diabetes [12]. Guanidine, the active compound, which was responsible for the relief of intense urination, was later discovered [13]. Metformin had been derived from a natural product without the knowledge of the molecular mechanism for disease, yet it proved to be a safe and effective therapy [12]. Recent studies have represented that metformin improves insulin resistance by reducing hepatic gluconeogenesis and by enhancing glucose uptake by skeletal muscle [14,15]. More specifically, metformin activates AMP-activated protein kinase (AMPK) which results in a number of actions including a decrease in glucose production in hepatocytes and an increase in glucose uptake in skeletal muscle [16]. There is an evidence that shows metformin accumulates within mitochondria at a concentration up to 100-fold higher than in the extracellular medium [13]. Metformin, which carries a positive charge, can be driven in to the mitochondria using the polarized property of both the cell and mitochondrial membrane (Fig. S1) [13]. Furthermore, metformin has been identified as a potential anti-cancer agent for its ability to inhibit tumor growth because of regulated insulin levels [17].

Mitochondrial accumulation of metformin itself led us to hypothesize that CDs which are derived from the metformin can also reserve the same property. Mitochondrial localization is a prominent and unique characteristic for any type of CDs because mitochondria plays a significant role in various cellular functions for instance generation of ATP and reactive oxygen species (ROS), intracellular calcium signaling, regulation of trans membrane potentials, maintenance of cellular redox, homeostasis and initiation of apoptosis and autophagy as a vital energy-supplying organelle within healthy and tumor cells [18,19]. Diseases, such as Alzheimer's, Parkinson's, diabetes and cardiac dysfunctions are directly related to dysfunctions at mitochondria so that tracking of mitochondrial state and behavior is critical for adjusting cellular fate and treating mitochondrial diseases [20]. Therefore, numerous commercial mitochondrial imaging biomarkers, including Mitotracker, Rhodamine 123, tetramethylrhodamine methyl ester, mitochondria-targeting green fluorescent protein (Mitochondria-GFP) and 5,5′,6,6′-tetrachloro-1,1′,3,3′-tetraethylbenzimidazolcarbocyanine iodide (JC-1), have been heavily studied for past decades [21,22]. However, these mentioned biomarkers usually suffer from the lack of modified functional groups, limited cellular permeability, poor water solubility, short tracking time, high cost or complicated staining procedures, which severely limit their applications in live-cell mitochondrial tracking [21]. Recently, various CDs have been synthesized as a promising alternative for mitochondrial targeting biomarkers [20,23,24]. Despite mitochondrial targeting properties of these CDs in vitro studies, they haven't been tested for blood–brain barrier (BBB) penetration feature to the best of our knowledge. Considering the diseases such as Alzheimer's, Parkinson's and brain tumors, BBB penetration is one of the crucial properties for CDs which are modified for diagnosis and treat trials of mitochondria related brain diseases.

Effective systems including nanoplatforms have propelled to the forefront in investigations of drug delivery to the brain [25,26]. However, drug delivery to the brain is still one of the main

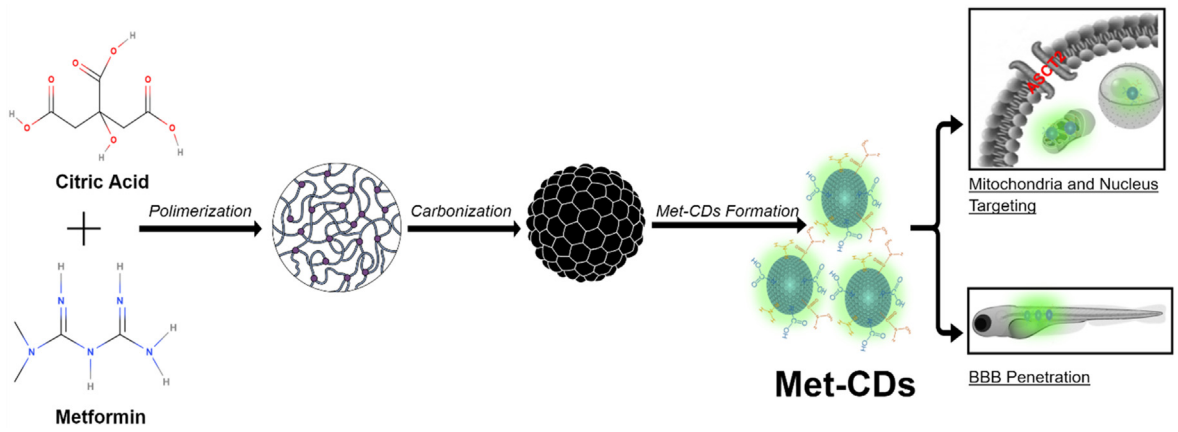

Scheme 1. Schematic representation for the synthesis of the Met-CDs.

challenges in medicinal chemistry because of the presence of the BBB. Tight junctions between endothelial cells of the BBB prevent the passage of therapeutic agents to pathological tissues in the brain [27]. There are several possible pathways for a molecule to cross the BBB including passive diffusion, or cell endogenous transport systems, such as carrier-mediated transport, receptor-mediated transport, or adsorptive-mediated transport [26]. Size also plays a role in a molecule's ability to cross the BBB. Small molecules or particles with sizes < 4 nm are prone to penetrate the BBB via passive diffusion through the gaps of 4–6 nm between the tight junctions [28]. Alternatively, amino acids, glucose and ketones, which are essential nutrients for cell activities penetrate through the BBB via carrier-mediated transports [29]. It has been shown by several studies that metformin can cross the BBB due to being a small cationic charged molecule [16,30,31].

This study introduces the synthesis of Met-CDs for the first time in the literature reference. We have designed a bottom-up synthesis approach for Met-CDs by using microwave-assisted method. Bioimaging studies extrapolated mitochondrial and nucleus targeting ability of Met-CDs. Subsequently, a zebrafish model was administered to test *in vivo* BBB penetration of Met-CDs. It has been observed that Met-CDs can cross the BBB possibly via a carrier-mediated transport system due to highly structural resemblance to glutamine. With unique mitochondrial targeting and BBB penetration abilities, Met-CDs are promising versatile nanocarriers and biomarkers for diagnosis and treatment of severe brain diseases such as Alzheimer, Parkinson, and brain tumors.

2. Experimental section

2.1. Materials

Anhydrous citric acid (purity > 99.5%) was purchased from VWR (West Chester, PA). Metformin hydrochloride (purity > 99%) was obtained from MP Biomedicals (Irvine, CA). For the dialysis of carbon dots and for the preparation of all solutions deionized water (DI) was used as solvent. It was purified by using a MilliQ3 water purification system obtained from Millipore Sigma (Burlington, MA). The surface tension of the purified deionized water is 72.6 $mN{\cdot}m^{-1}$ with a resistivity of 18 MΩ·cm and a pH of 6.6 ± 0.3 at 20.0 ± 0.5 °C. All the chemicals were used as received. Spectrapor dialysis tubing with a molecular weight cutoff (MWCO) of 100–500 Da was purchased from VWR (West Chester, PA). Human embryonic kidney cell line HEK293 was procured from the American Type Culture Collection (ATCC, Manassas,VA, U.S.A.). Pediatric glioblastoma cell line SJGBM2 was acquired from the Children's Oncology Group (COG, Lubbock, TX) and U87 (adult glioblastoma cell line) was obtained from the American Type Culture Collection (ATCC, Manassas,VA, U.S.A.). Additionally, other two pediatric high-grade glioma cell lines, called Diffuse Intrinsic Pontine Glioma (DIPG) NP53 which was generated from genetically engineered mouse (*GEM*) tumor model, and KNS42 were provided by Dr. Oren Becher (Nortwestern University, Chicago, IL) and by Dr. Chris Jones (The Institute of Cancer Research, London), respectively. Dorsal root ganglion cultures for non-tumor bioimaging studies were generously provided by Yelena Pressman (University of Miami, FL). Sea urchins *(Lytechinus veriegatus)* were provided by the Duke University Marine Lab (Beaufort, NC, U.S.A).

2.2. Synthesis of the Met-CDs

Met-CDs were synthesized via a microwave-mediated method. Using 1: 1 M ratio between the precursors, 500 mg of metformin hydrochloride (MW = 165.63 g/mol) and 582 mg of citric acid (MW = 192.12 g/mol) were dissolved in 25 mL of DI water and stirred for 30 min. Then, the mixture was heated for 3 min in a domestic microwave oven of 1000 W. After the reaction was completed, brown-black solid was collected from the bottom of the beaker. The collected solid was dispersed in about 15 mL of DI water and sonicated for 30 min. Then, the sonicated dispersion was centrifuged at 6000 rpm for 30 min at 19 °C to remove any precipitates. To eliminate any remaining large particles, the supernatant of the centrifuged solution was then filtered through a 0.2 μm filter membrane (VWR, US). Then, the filtrate was dialyzed against DI water for 3 days using 100–500 Da MWCO dialysis tubing changing the dialysis water every 24 h. Finally, sample was lyophilized using a FreeZone 4.5 L cascade benchtop freeze dry system (Labconco, Co.; Kansas City, MO).

2.3. Characterization of the Met-CDs

Met-CDs (50 $\mu g\ mL^{-1}$) in aqueous medium were first characterized by UV–vis absorption spectroscopy in a 1 × 1 cm quartz cell (Starna Cells, Inc.; Atascadero, CA) using a Cary 100 UV–vis spectrophotometer (Agilent Technologies, USA). Subsequently, fluorescence emission spectra of the aqueous dispersion of Met-CDs were acquired by using Horiba Jobin Yvon Fluorolog-3 with a slit width of 5 nm for both excitation and emission. Then, Met-CDs were further characterized via solid FTIR spectroscopy utilizing a Perkin Elmer FTIR (Frontier, US) spectrometer equipped with the attenuated total reflection (ATR), which operates the ATR prism alone as the background. For the approximate molecular weight (MW) determination of Met-CDs, Matrix-Assisted Laser Desorption/Ionization-Time of Flight (MALDI-TOF) mass spectrometry (MS) was performed using a Bruker auto flex speed spectrometer. For the nanoparticle size-distribution-and morphological characterizations of Met-CDs, TEM studies were achieved with a JOEL 1200 × TEM and AFM studies were conducted using an Agilent 5420 atomic force microscope in the tapping mode. For the zeta potential measurement of Met-CDs, a DLS nano series Malvern Zetasizer (Westborough, MA) was used. X-ray photoelectron spectra (XPS) were acquired using a Perkin Elmer PHI 560 system with a double-pass cylindrical mirror analyzer operated using a Mg Kα anode with a hν = 1253.6 eV photon energy operated at 250 Watts and 13 kV. Met-CD samples were mounted as a powder onto a custom-built sample holder and inserted into the XPS system via turbo pumped antechamber. The observed C 1 s core level at 284.9 eV emanating from the C=C alkenyl Met-CDs as previously measured in our laboratory was used as a binding energy (BE) reference [32–35]. Core level intensities of the O 1 s and C 1 s orbitals were normalized using their known atomic sensitivity factors [36]. XPS peaks were curve fitted using 70-to-30% Gaussian-Lorentzian line shapes with Shirley background subtractions [37]. BE peak envelopes were deconvoluted using Casa XPS ver. 2.2.107 (Devonshire, UK) software. Different batches of Met-CDs were studied by repeating each characterization method to validate the reliability of the data and the reproducibility of the CDs.

2.4. Fluorescence quantum yield calculations

The fluorescence quantum yield (Φ) of Met-CDs was calculated by comparing the integrated area under the fluorescence curve and the absorbance intensity values using quinine sulfate and harmane as the reference standards. It has been shown that quinine sulfate and harmane have 54 and 83% quantum yield (QY), respectively when they are dissolved in 0.1 M H_2SO_4 (refractive index, n_R = 1.33, at 350 nm) [38,39]. Additionally, Met-CDs were dispersed in DI water (refractive index, n_R = 1.33). Then, UV–vis absorbance measurements of the samples in the 1 cm path length cuvette were acquired maintaining the absorbance intensity under 0.05 at 350 nm. Following to absorbance readings, fluorescence

emission spectra of Met-CDs and standards were obtained with the 350 nm excitation wavelength. Average of absorbance intensities and integrated areas for the fluorescence emission spectra were used in the following equation, Eq. (1):

$$\Phi = \Phi_R \times (I/I_R) \times (A_R/A) \times \left(n^2/\ n_R^2\right) \quad (1)$$

In this equation, Φ_R, *I*, A, n symbols illustrate the literature QY of the standard, the integrated area under the PL curve, absorbance intensity at 350 nm, and the refractive index, respectively. Subscript R is denoted for the reference.

2.5. Quantifying the number of primary amine groups on the surface of the Met-CDs

A fluorescence analysis using fluorescamine assay has been performed to calculate the number of primary amine groups on the surface of the Met-CDs. Here we followed the work which has been published by Zhou et al. [33] 2 mg of Met-CDs was dispersed in 2 mL acetone/ 1 × PBS buffer solution with volume ratio 1:1. Next, a mixture of 50 μL of the Met-CDs dispersion and 0.5 mg fluorescamine was prepared in a 5 mL volumetric flask which was then filled with the same acetone/ 1 × PBS (1:1) buffer solution. Each solution was diluted 100 times in the end to prevent the error caused by the emission saturation. The linear relationship between the molarity of primary amine group and the fluorescence intensity along with the addition of 1,2-ethylenediamine (EDA) into fluorescamine was studied for the quantification of the number of primary amine groups on the surface of the Met-CDs. The fluorescence intensity which was produced upon the addition of fluorescamine into Met-CDs aqueous dispersion was incorporated into the linear equation relationship. By using this equation, we calculated the amount of primary amine groups on the surface of the 2 mg Met-CDs.

2.6. Cytotoxicity studies of Met-CDs with sea Urchins, HEK-293 human embryonic kidney and High-Grade glioblastoma cell lines

Two models, the sea urchin animal model and human HEK-293 embryonic kidney cell line in vitro model, were evaluated for the cytotoxicity studies. Fertilized *Lytechinus variegatus* sea urchin eggs were plated in a 24-well plate. Each well contained 100 embryos in 200 μL of filtered seawater. Then, the embryos were treated with different concentrations (0, 10, 25, 100 μM) of Met-CDs which were dispersed in 400 μL of seawater. The plate with Met-CDs treatments was then incubated at 21 °C. Observations for the percentage of survival was done after 24 h post fertilization at the gastrula stage. For each concentration, three biological replicates were performed.

For the human embryonic kidney cell line experiment, HEK-293 (0.5×10^5) cells were grown in a 96-well plate and incubated at 37 °C with 5% CO_2 in 100 μL of Dulbecco's Modified Eagle's Medium high glucose medium containing 1% penicillin/streptomycin (both from Gemini Biosciences, West Sacramento, CA) and supplemented with 10% of fetal bovine serum for 24 h. Then, cells were treated with 100 μL of different concentrations (0, 10, 25, 100 μM) of Met-CDs. Cell viability was calculated by using the CellTiter 96 Aqueous One Solution Cell Proliferation Assay (MTS) (Promega Madison, WI). Cell viability was determined with MTS assay after 72 h of incubation. Absorbance was measured at 490 nm using BioTek Synergy HT plate reader.

Further cytotoxicity effects of Met-CDs were evaluated towards pediatric brain tumor cell lines and an adult brain tumor cell line. Cell viability results were determined using the MTS assay as previously described. Briefly, we plated cells into 96-well plates at 0.5×10^5 per well, 24 h prior to drug treatment. Afterwards, cells were treated with different concentrations (0.1, 1, 10, 25 μM) of Met-CDs. After 72 h incubation, cell viability was determined using same MTS assay described for HEK-293 cells. The absorbance was taken at 490 nm using a BioTek Synergy HT Plate reader. Average of 3 separate experiments were calculated to present the data in which the viability was calculated as the relative percentage of non-treated cells. Standard error of the mean (SEM) was calculated. The consistency and reproducibility of the data was confirmed using different batches of Met-CDs.

2.7. In vitro bioimaging

SJGBM2 and Hek-293 cells were grown at 4-well plates (NUNC, Denmark) for imaging at a density of 1×10^5 and 0.5×10^5, respectively in 750 μL Roswell Park Memorial Institute medium (RPMI) and incubated for 24 h for sufficient cell growth. Then, the media was aspirated out, cells were treated with 500 μL RPMI solutions containing 5 and 2.5 mM of Met-CDs and further incubated for 5 min, 1 h and 24 h. After the treatment, media with Met-CDs was aspirated out and cells were retreated in 500 μL RPMI with 0.1 μM Red Mitotracker (Thermo Fisher Scientific, Waltham, MA) for 45 min based on the manufacturer's instructions. Once all the treatments were finished, cells were washed with PBS and fixed with fresh 4% paraformaldehyde for another 30 min. Subsequently, fixed cells were washed with PBS solution two more times and one drop of antifade reagent with DAPI (Thermo Fisher Scientific, Waltham, MA) was added on the top of the cells. For each well, one cover slip was added carefully on top before imaging. A Leica SP5 confocal microscope (Leica Microsystems Inc., Buffalo Grove, IL) employed by using fluorescent channels with the excitation wavelength of Blue and Green, 405 nm, Red, 561 nm. Emission ranges: Blue, 441–481 nm, Green, 480–520 nm, Red, 579–619 nm. Same settings were used for each group.

Dorsal root ganglion (DRG) cultures were isolated from the embryonic stage 15 pregnant rat similar as described in Sleigh's paper for non-tumor neuronal bioimaging studies [40]. DRG neurons were isolated from the dorsal root ganglia of embryonic rats (E15) and plated on poly-L-lysine/laminin coated 24-well (Corning, NY, US) plates in neurobasal media supplemented with B-27, L-glutamine and nerve growth factor (Gibco). Cultures were treated with 10 μM fluorodeoxyuridine to prevent the proliferation of contaminating cells such as fibroblasts and schwann cells. Neurons were treated with 2.5 mM concentration of Met-CDs for 24 h one week after isolation. After the treatment, neurons were washed with PBS and pre-fixed with couple of drops of fresh 4% paraformaldehyde for 5 min. Media with PBS and paraformaldehyde were aspirated gently with an aspirator pipet. Neurons were further fixed with fresh 4% paraformaldehyde for 10 min. After fixation was completed, neurons were further washed twice with PBS and one drop of antifade reagent with DAPI (Thermo Fisher Scientific, Waltham, MA) was added on the top of the cells. One cover slip was inserted carefully on top of each well before imaging on a Floid Cell Fluorescent Microscope (Thermo Fisher Scientific, Waltham, MA).

2.8. Immunocytochemistry

To assess the presence of the dorsal root ganglion neurons, immunocytochemistry was performed using two primary antibodies, neurofilament (Developmental Studies Hydridoma Bank, Iowa City) and β-tubulin (Cell Signaling Technology, Danvers, MA), and two secondary antibodies, Alexa Fluor 594 goat anti-mouse and Alexa Fluor 488 goat anti-rabbit (Thermo Fisher Scientific, Waltham, MA). Neurons were plated on poly-L-lysine/laminin coated four-well plates in neurobasal media supplemented with B-27, L-glutamine, and nerve growth factor (Gibco; Thermo Fisher

Scientific, Inc., Waltham, MA, US). Then, neurons were fixed in 4% paraformaldehyde, blocked and permeabilized with a 5% bovine serum albumin (BSA) with 0.6% Triton-X 100 and then treated with the primary antibodies neurofilament (Thermo Fisher Scientific, Waltham, MA) and β-tubulin (Cell Signaling Technology, Danvers, MA). A negative control was included for all antibodies tested. These neurons were incubated with only the antibody diluent (2.5% BSA, 0.3% triton, balance PBS). Neurons were then treated with a fluorochrome conjugated secondary antibodies Alexa Fluor 594 goat anti-mouse and Alexa Fluor 488 goat anti-rabbit (Thermo Fisher Scientific, Waltham, MA) followed by antifade reagent with DAPI (Thermo Fisher Scientific, Waltham, MA). Samples were imaged under a Floid Cell Fluorescent Microscope (Thermo Fisher Scientific, Waltham, MA).

2.9. Zebrafish injection and bioimaging for crossing the BBB.

Wild-type zebrafish (5 days post fertilization) were acquired from the Zebrafish Core Facility at University of Miami. 2 mg of Met-CDs was dispersed in 1 mL of DI water and this dispersion was injected into the hearts of the seven zebrafish which were previously anesthetized by tricaine. Subsequently, 10 min after injection, a bioimaging was performed on the injected zebrafish using a Leica SP5 confocal microscope under white light and excitation at 405 nm (for Met-CDs). University of Miami Animal Care and Use Committee approved the animal care protocol for all the procedures performed in this study which also abides the guidelines of the National Science Foundation [35].

2.10. Statistical analysis

Significance of cytotoxicity and cell viability studies were determined using Student's t-tests for all pairwise comparisons of the different treatments that were tested. All the results are mentioned as the mean ± standard error of the mean (SEM). Significance was set at $p < 0.05$.

3. Results and discussion

3.1. Characterization of Met-CDs

Met-CDs were prepared as described in the experimental section. Purification step for the CDs synthesis is one of the most crucial steps not only to get rid of all starting materials which did not react during the Met-CDs synthesis, but also eliminate all the unwanted fluorophores which can affect the fluorescent properties of synthesized Met-CDs. Considering the importance of the purification step, three different purification methods namely, centrifugation, syringe filtration and dialysis, were implemented for the purification of Met-CDs. Prior research about the formation of nitrogen doped CDs substantiates the belief that formation mechanism of these CDs includes polymerization as a first step and carbonization steps, subsequently [41]. From this perspective, we hypothesized that there is a condensation reaction between the amine groups of metformin and terminal carboxylic component of citric acid. Reaction between these two groups produce a carbon–nitrogen bond, creating a singular amide linkage which also yields a polyamide formation. After the polymerization step, as the heating process continues, carbonizations of these polymers occur and finally result in Met-CDs formation. UV–vis spectrum of Met-CDs showed a cha-racteristic absorption band at 340 nm (Fig. 1a). More specifically this band is a characteristic band for almost all nitrogen doped CDs because previous studies also have attributed the bands around 300–450 nm to $n - \pi^*$ electronic transition of C—N and C═N groups [42–44]. Additionally, there were two more absorption bands at 225 and 275 nm. The absorption band at 225 nm was assigned to $\pi - \pi^*$ electronic transition of C═C groups and the absorption band at 275 nm was attributed to $n - \pi^*$ electronic transition of C═O groups. C═C is one of the fundamental functional groups present in CDs and, similarly, C═O groups are oxidized version of constitutional C—C and C═C groups so it is expected to see both these electronic transitions in the UV–vis absorption spectra for any type of CDs. XPS analysis has shown the same phenomenon by displaying 86.4% of C 1 s levels in the core structure of Met-CDs. As shown in the Fig. 1b, Met-CDs possess an excitation-dependent PL emission in the range of 430–580 nm with the respective excitation at 360–540 nm. The PL maximum emission is at 450 nm when excited at 360 nm. Additionally, a red shift for this emission peak could be seen with increasing excitation wavelengths (Fig. S2). The mechanism behind the excitation dependent PL behavior of CDs remains largely debated. However, this behavior is commonly attributed to the presence of surface electronic states, incorporation of fluorophores into the particles structure, and dot-to-dot variations that ultimately lead to excitation-dependent ensemble properties [45]. Fluorescence Quantum Yield (QY) is one of the most significant parameters in the characterization of any type of CDs for various biomedical applications such as bioimaging and biosensing [46–48]. Along with its importance, QY calculations require lots of assays and consistent experimental setups to acquire reliable and valid results. Therefore, choosing appropriate standards and using at least two standards for the calculations are one of the most crucial points for the QY calculations. It is also important to match the emission range of the standards with the samples' emission range to minimize standard based errors. Additionally, using two standards gives possibility for cross-calibration and average standard deviation calculations of the experimental setup. Moreover, excitation wavelength of PL emission spectra is also one of the crucial parameters for QY calculations to decrease errors caused by acquiring tendentious PL emission spectra. Thus, excitation wavelength for PL emission spectra of both standards and sample was kept at 350 nm (to align with the literature reference QY values of our standards) and emission range was between 400 and 600 nm. In this study, the QY of the standards were cross-calibrated before the quantum yield calculations of Met-CDs to confirm the validity of our method for reliable results. From the cross-calibrations, QY of quinine sulfate and harmane were calculated as 55 (literature Φ = 54%) and 81.5 (literature Φ = 83%), respectively [38,39]. These results for the standards were close to their literature QY so that our method was reliable with ± 1% deviations. After confirming similar results for the standards with different batches, Met-CD samples were dispersed in DI water for the QY calculations. The same protocol was performed for the QY calculations of the Met-CDs by using two standards. As a result, quantum yield of the Met-CDs was calculated as 8.4%.

For the identification of functional groups in Met-CDs structure, FTIR spectroscopy was exploited in the solid state using an ATR accessory. Carboxylic (peaks at 3232 and 1716 cm^{-1}) and amine (peaks at 3365, 1195 and 1068 cm^{-1}) groups were detected on the surface of Met-CDs (Fig. 1c). Broad bands at 3365 and 3232 cm^{-1} were assigned to N—H stretching and O—H stretching, respectively. Then, bands at 2962 and 2779 cm^{-1} were attributed to C—H stretching. The rest of the peaks at 1716, 1570, 1519, 1401, 1195, 1068 and 822 cm^{-1} were identified in this order C═O stretching, N—H bending, N—O stretching, O—H bending, C—N stretching, and N—H (dimer) stretching. It is worth to note that both precursors do not have N—O bond in their structures, but presence of N—O bond was confirmed with FTIR spectrum of Met-CDs. This observation could be associated with proposed synthesis mechanism of Met-CDs. More specifically, polymerization and carbonization of both precursors might have resulted in

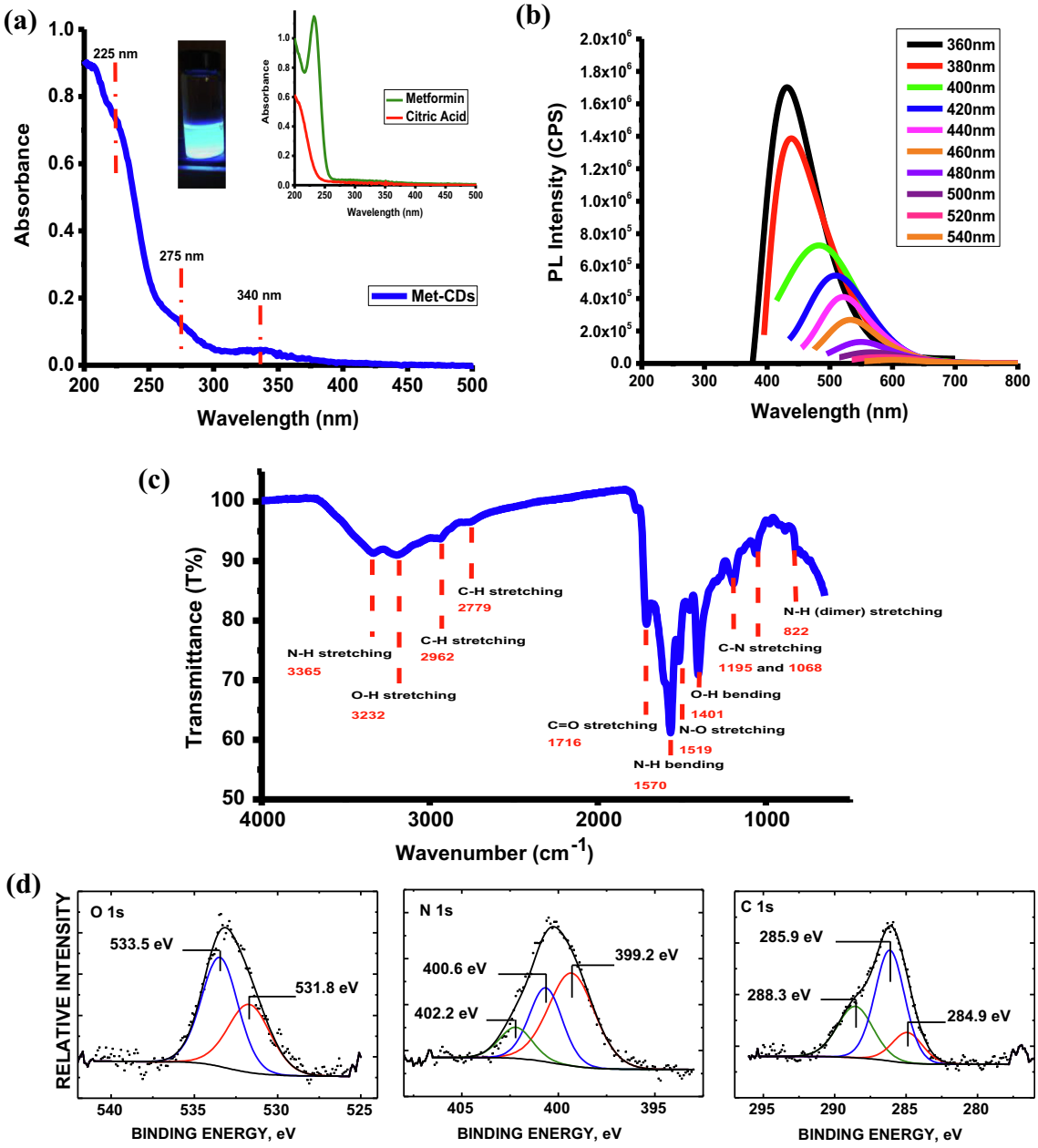

Fig. 1. (a) UV–Vis absorption spectrum of Met-CDs (concentration = 0.1 mg/ml). Inset, UV–Vis spectra of precursors namely, metformin and citric acid. (b) PL emission spectrum of Met-CDs (concentration = 1×10^{-6} mg/ml). (c) FTIR spectrum of Met-CDs. (d) XPS core levels of O 1 s, N 1 s and C 1 s orbitals of Met-CDs.

formation of N—O vibrational mode for the FTIR spectrum of Met-CDs.

For further investigation of the surface functional groups on the Met-CDs, XPS were applied on Met-CDs. Fig. 1d deduces XPS core levels for the C 1 s, N 1 s and O 1 s orbitals of the Met-CDs. Atom % mole fractions of C, O and N were 84.6, 8.0 and 7.4%, respectively. Measured binding energies (BEs) (with fwhm, relative oxidation state % area in parentheses) of the C 1 s core level were at 284.9 eV (2.5, 15.3%), 285.9 eV (2.4, 54.4%) and 288.3 eV (2.9, 30.3%), signifying the alkenyl C=C, alcohol (—OH) and carboxylic acid (—COOH) on the surface of Met-CDs, respectively [49,50]. The O 1 s core levels for this sample showed BE peak centers (with fwhm, relative oxidation state % peak areas in parentheses) at 531.8 eV (3.0, 42.0%) and 533.5 eV (2.5, 58.0%), consistent with amide C=O and ether type O atoms in ester group, respectively [35]. The BE for N 1 s core levels for this sample displayed 399.2 eV (2.8, 55.2%), relating to an aliphatic primary amine N—H [50]. In addition, we assigned the N 1 s core level BEs at 400.6 eV (2.0, 31.6%) and 402.2 eV (2.0, 13.2%) to pyrrolic N, and hyponitrite (NO) in the Met-CD structure, respectively [51,52]. As mentioned before Fig. 2b exhibited various functional groups, O—H (3232 cm^{-1}) and C=O groups (1716 cm^{-1}), within the Met-CDs as observed by the FTIR. These data corroborate XPS BE peaks assignments for the aliphatic N—H (1570 cm^{-1}) and N—O groups (1519 cm^{-1}) within the sample. After confirming the presence of amine groups on the surface of Met-CDs by using different techniques, we calculated the number of primary amine groups on the surface of Met-CDs by using fluorescamine assay. Using the same protocol as Zhou et al. the number of primary amine group on the surface of Met-CDs was found to be 0.050 ± 0.005 mol/g [33]. It is also important to indicate that the zeta potential of Met-CDs was measured as +0.45 mV. Positive charge on the surface

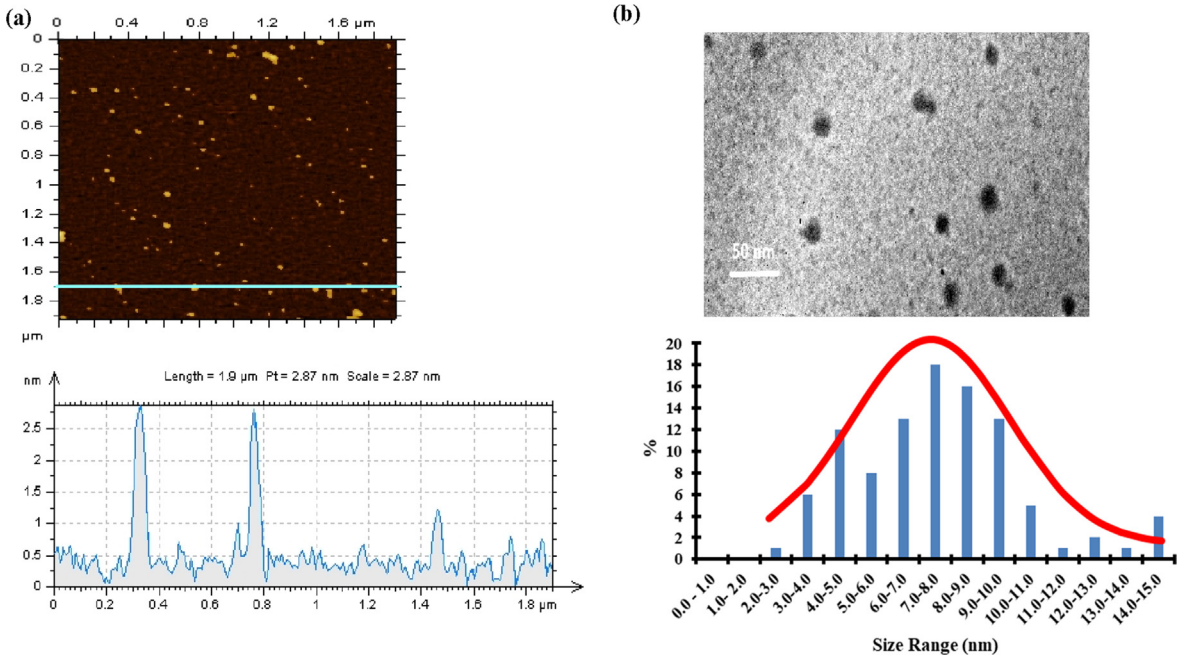

Fig. 2. (a) AFM image and height profile of Met-CDs. Scale = 2.87 nm in AFM profile extraction graph represents the height of the tallest particle at z-dimension under blue line that has been drawn on the AFM image. (b)TEM image and histogram of Met-CDs fitted with gaussian size distribution. Scale bar is 50 nm. (n > 300). (For interpretation of the references to color in this figure legend, the reader is referred to the web version of this article.)

of Met-CDs could be related to the presence of abundant ammonium ions.

AFM and TEM images of Met-CDs were attained to understand the morphology and size distribution of the Met-CDs (Fig. 2a and b). Herein, TEM provides the most accurate estimation of the Met-CDs homogeneity in × and y dimensions and AFM allows the characterization of the Met-CDs height in z-dimension [53]. Size histograms were generated with different batches of Met-CDs. To prevent any particle aggregation, all Met-CD samples were sonicated for 30 min prior to obtain AFM and TEM images. Met-CDs presented a narrow size distribution with a mean height of 3 nm for the AFM images. On the other hand, we observed a wider and asymmetric gaussian distribution in the range of 2–15 nm for the TEM images. Thus, the average size is measured to be around 6–7 nm according to the measurements of more than 300 dots. Considering mean particle sizes from the results of two different microscopic techniques, we observed that Met-CDs have a spherical shape and an average diameter around 5–6 nm. Additionally, the MW of the Met-CDs was found to be around 633 Da by MALDI (TOF) mass spectrometry (Fig. S3). Thus, 100–500 Da MWCO membrane was selected to be used for the dialysis of Met-CDs.

3.2. Cytotoxicity study

CDs are one of the most popular nanomaterials since their discovery because studies have shown that they have high biocompatibility and are minimally toxic towards non-tumor cells [54,55]. Especially for bioimaging applications, CDs are preferred over traditional toxic biomarkers such as metal-based quantum dots due to their unique biocompatibility. To study cytotoxicity and biocompatibility of Met-CDs, cell viability studies were conducted using two models: sea urchin embryos and cell lines with non-tumor and tumor cells. Here, two models employed for the cytotoxicity studies because we wanted to increase the reliability of the results. Additionally, since Met-CDs were planned to study for live cell bioimaging studies, it is important to test their toxicity towards both the tumor and non-tumor cell lines. More specifically, bioimaging is defined as a noninvasive process of visualization of biological activity in a specific period [56]. Any live cell bioimaging materials should be non-toxic towards the targeted cell line because cells need to protect their cell membrane integrity [57]. When cells start to die, their cell-membrane will become impaired and it will uptake anything in the media [58]. We hypothesize that Met-CDs will be good candidate for bioimaging studies because they can be non-toxic towards both the tumor and non-tumor cells so that cells can protect the unity of their cell membrane. It is well-known that the sea urchins *(Strongyloentrotus purpuratus)* embryos demonstrate acute toxic sensitivity [42]. As described before; sea urchin embryos were treated with different concentrations of Met-CDs. There was no significant cell death after Met-CDs treatments ($p > 0.05$). Fig. 3a presents that the embryos kept their normal development even at the highest concentration (100 µM) of Met-CDs tested. Furthermore, a significant cell death also was not observed for HEK-293 cytotoxicity studies even with the highest concentration (100 µM) of Met-CDs tested (Fig. 3b). HEK – 293 are non-tumor embroyonic kidney cells, so two non-tumor models, sea urchin embryos and HEK- 293 cells, yielded no significant cell deaths indicating that Met-CDs have very low toxicity and good biocompatibility towards these non-tumor models. After confirming that Met-CDs are non-toxic towards non-tumor cells, Met-CDs were further tested for their toxicity towards the cancer cells. In this study, high-grade glioma cell lines namely, pediatric glioblastoma cell lines KNS-42 and SJGBM-2, adult glioblastoma cell line U-87 and the mouse DIPG cell line NP53 were chosen. We have compared the cytotoxicity of Met-CDs with metformin molecule alone and Met-CDs exhibited complementary cell viability results as metformin molecule (Fig. 3c and S4). However, there was no statistically significant cancer cell death for both treatments at the concentrations tested. Our hypothesis was that "Met-CDs will be good candidate for bioimaging studies because they can be non-toxic towards both tumor and non-tumor cells" and it was supported by the cytotoxicity results of both non-tumor and tumor cells at the concentrations tested. It is worth to mentioning that metformin molecule has indirect

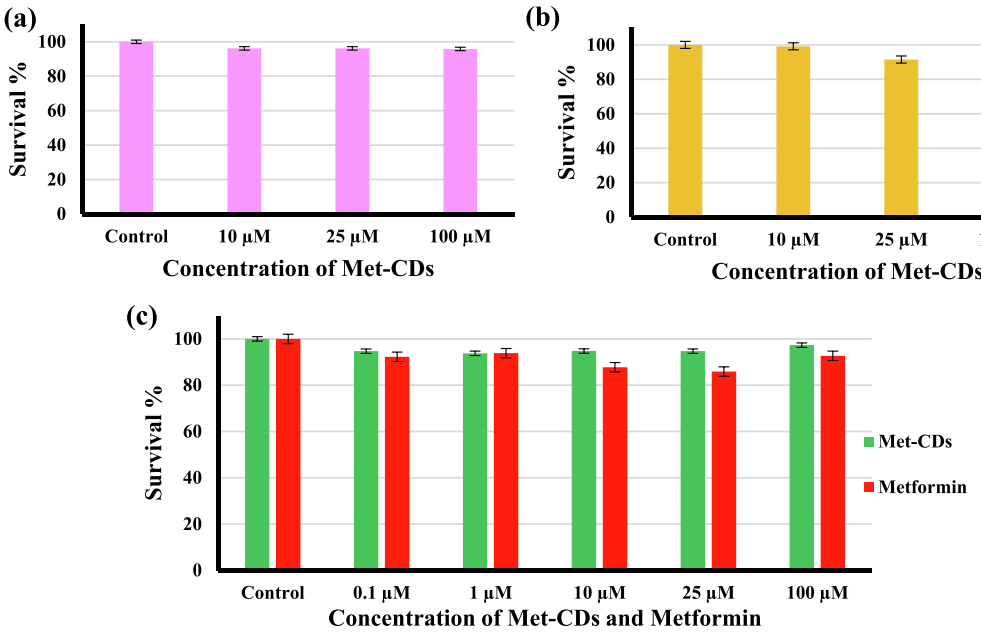

Fig. 3. Cytotoxicity studies of Met-CDs. (a) Sea Urchin cytotoxicity results. b) HEK-293 cytotoxicity results. (c) SJGBM-2 cell line cytotoxicity results. Results are expressed as %of survival rate. Values are means ± SEM (n = 12). P > 0.05 so there was no significant difference from %survival rate of control groups.

effect to decrease the growth rate of cancer cells due to regulating mitochondrial activities within the cancer cell, it enhances therapeutic response of any drugs that present in the medium [59–61]. From this point, Met-CDs displayed similar cell viability results as metformin alone so that there is a high possibility for Met-CDs to exhibit similar enhancement effects with the presence of any other therapeutics. Since Met-CDs possess abundant number of available functional groups on their surface, conjugation of these therapeutics is possible on the surface of Met-CDs. This means that when Met-CDs are conjugated to a drug, they will act as not only nanocarriers but also therapeutic effect enhancers.

3.3. In vitro bioimaging and organelle staining studies

As mentioned in the previous section, Met-CDs showed low cytotoxicity towards both tumor and non-tumor cell lines at the concentrations tested. Great biocompatibility along with, good water dispersibility and excellent PL properties that make Met-CDs a suitable candidate for bioimaging applications. Since the Met-CDs have excitation dependent PL emission, cells can be imaged by using different fluorescence channels. In this study, green channel was selected to image the cells because living cells and organisms have autofluorescence that emits in the blue channel due to presence of NADPH, proteins, and other amino-functional fluorophores [62]. Preliminary experiments were conducted with different concentrations of Met-CDs to detect optimum concentrations. Here, we selected HEK-293 (non-cancer embryonic human kidney), DRG (non-cancer) neuronal and SJGBM2 (High-grade glioblastoma) cell lines to proceed with imaging studies to compare cell uptakes of Met-CDs in cancer versus non-cancer cell lines. HEK-293, and SJGBM2 cells and DRG neurons were treated with 500 µL of 2.5 mM Met-CDs. After 24 h incubation, cells were imaged under the fluorescent microscope keeping the experimental settings constant for each image. Met-CDs did not change the cell shape and viability. Moreover, luminescence intensity for the HEK-293 (non-cancer) cells and DRG (non-cancer) neurons were observed to be lower than the SJGBM2 (cancer) cells, suggesting that Met-CDs' cell uptake was higher with SJGBM2 (cancer) cells (Fig. 4a, b and c). Control experiments of these three cell imaging studies were also performed and there was no autofluorescence from the cells under these imaging settings (Fig. S5). When the possible cell entering mechanism of Met-CDs was considered, diffusion was the initial possibility that could be discussed because Met-CDs possess small size and slightly positive charge. However, after seeing these results, we hypothesized that diffusion is not the only possible mechanism of Met-CDs to cross the cell membrane. It has been well known that cancer cells take up more nutrients from the environment than healthy cells to support their uncontrolled proliferation [63]. Amino acids are one of these key nutrients. For instance glutamine which is the most abundantly available amino acid in the blood, fuels biosynthetic processes such as ATP generation, redox homeostasis, nucleotide, protein, and lipid synthesis [63]. Hence, the amine, amide and carboxylic acid surface functional groups of Met-CDs highly resemble the glutamine structure. We hypothesize that cancer cells uptake more Met-CDs than healthy cells due to this resemblance. Additionally, glutamine enters the cancer cells via glutamine transporter SLC1A5 (ASCT2) which has gene expression in pediatric high-grade gliomas (pHGG) much higher than non-tumor cell lines (Fig. S6) [64]. From this point, Met-CDs could penetrate the cell membrane of cancer cells as metabolic substrate (glutamine via the ASCT2 transporter). For the immunocytochemistry study, two primary antibodies (neurofilament and β-Tubulin), two secondary antibodies (Alexa Fluor 594 goat anti-mouse and Alexa Fluor 488 goat anti-rabbit) were used to detect the presence of the DRG neurons. Fig. 4d and f show that with the treatment of primary and secondary antibodies, neurons exhibited excellent fluorescence under both green and red channels indicating the presence of primary rat neuronal cells. To confirm this fluorescence derived from the interactions between neurons and antibodies, negative controls with secondary antibodies and DAPI was accomplished (Fig. 4e and g). Since the secondary antibodies give fluorescence only at the presence of primary antibodies, we did not observe any fluorescence for control groups under green and red channels confirming that there was no non-specific fluorescence of antibodies or autofluorescence of the neurons.

Further interpretation was deduced from the results of this imaging study. As can be seen from Fig. 4c, there were specific

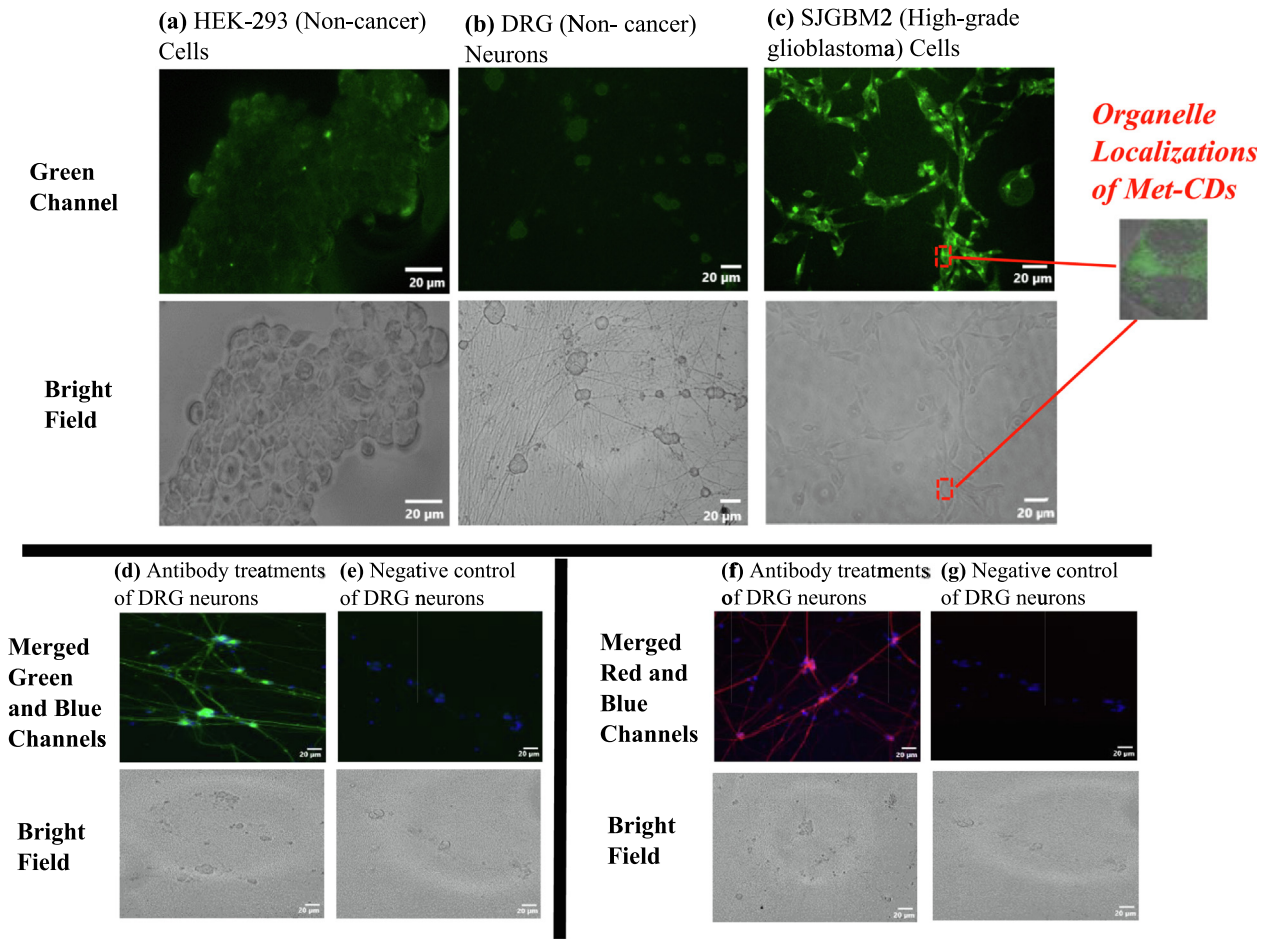

Fig. 4. Fluorescence microscopy green and bright channels images of a) HEK-293 (Non-cancer embryonic kidney) cells. b) DRG (non-cancer) neurons. c) SJGBM2 (High-grade glioblastoma cancer) cells. All the three types of cells were treated with 2.5 mM Met-CDs for 24 h. Immunohistochemistry fluorescence microscopy images of d) DRG neurons treated with β-Tubulin (Primary antibody). e) Negative control of DRG neurons treated with Alexa Fluor 594 goat anti-mouse (Secondary antibody), and DAPI. f) DRG neurons treated with Neurofilament (Primary antibody) and DAPI. g) Negative control of DRG neurons treated with Alexa Fluor 488 goat anti-rabbit (Secondary antibody) and DAPI. Both d and e were imaged under the overlayed green and blue channels and f and g were imaged under the overlayed red and blue channels. During the imaging process, all experimental settings such as contrast, brightness, light intensity were kept same for each image. Scale bars are 20 μm. Excitation wavelengths: Blue, 358 nm, Green, 488 nm. (For interpretation of the references to color in this figure legend, the reader is referred to the web version of this article.)

organelle localizations of Met-CDs inside only SJGBM2 (High-grade glioblastoma) cells. However, a specific localization was not observed in non-cancer cells or neurons. Three more experiments with the same conditions were performed and same localizations of Met-CDs were monitored in each experiment. Our first hypothesis was that these localizations happened inside the mitochondria because metformin's main mechanism of action arises inside the mitochondria. Concisely, metformin decreases mitochondrial respiration which results in energetically inefficient cells [65]. Thus, Met-CDs might keep the same features as metformin and localize inside the mitochondria due to presence of metformin moieties on the surface of Met-CDs. In addition to mitochondrial localization, we expected to see some localizations inside the nucleus because metformin has direct effects related to the adenosine monophosphate (AMP) – activated protein kinase (AMPK) inside the nucleus [66]. To test our hypotheses about mitochondrial and/ or nucleus localization of Met-CDs, mitochondria and nucleus staining experiments were employed using Mitotracker red and antifade agent with DAPI. Here, Mitotracker red was selected to image mitochondria of SJGBM2 cells at the red channel and antifade agent with DAPI was decided to image nucleus of SJGBM2 cells at the blue channel. There were no PL leakages between these channels. In other words, each channel imaged only the targeted biomarker (Green, Met-CDs, Red, Mitotracker, Blue, DAPI- Nucleus) under the confocal microscope. During the imaging stage, all settings were kept constant for each image. For the control group, cells were treated with only Mitotracker and DAPI without any Met-CD biomarkers, so that there was no PL emission at the green channel (Fig. S7). On the other hand, for Met-CD treatments, bright PL emission was observed through the whole cell structure along with specific localizations at the green channel. These localization patterns of Met-CDs at the green channel matched perfectly with the localization patterns of mitochondria at the red channel (Fig. 5a, b). When merged green and red channel was analyzed, an orange color PL emission was observed confirming that the overlap between the localization patterns of Met-CDs and mitochondria. Met-CDs were capable of selectively localizing inside the mitochondria of SJGBM2 tumor cells and emitting bright PL in wavelength of the green region, especially after 1 h of treatment. When Fig. 5a and b are compared, it could be interpreted that Met-CDs initiated beginning periods of the mitochondrial localizations with more homogenous distribution throughout the cell structure, but after 24 h of incubation with Met-CDs, mitochondrial localizations were much more advanced.

More bioimaging studies were conducted to analyze how Met-CDs were distributed inside the cells for shorter periods, such as 5 min. SJGBM2 cells treated with 5 mM Met-CDs for 5 min. Same as previous imaging study, green and blue channel were employed

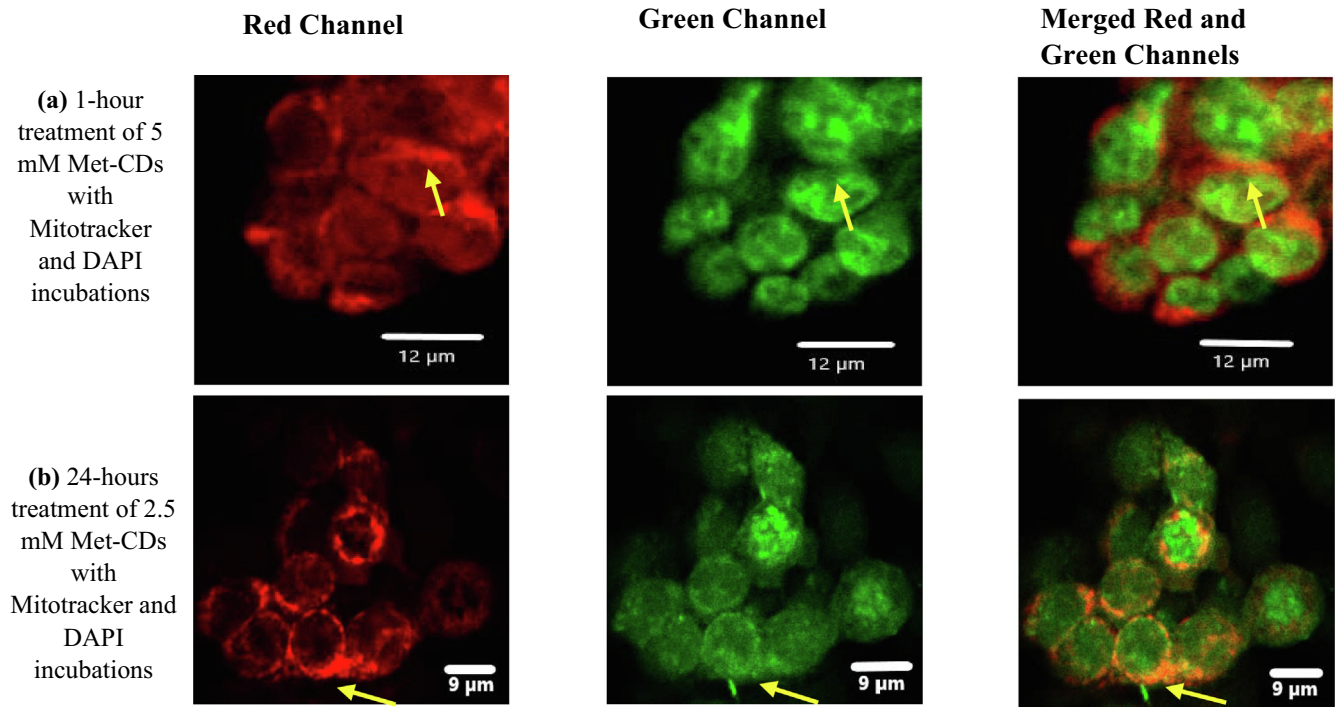

Fig. 5. Confocal images of SJGBM2 tumor cells after incubating with Met-CDs and Mitotracker for 1 h and 24 h. (a) Beginning period of co-localization of Met-CDs (5 mM, Ex = 405 nm) and mitochondria (visualized by 0.1 μM Mitotracker, Ex = 561 nm) after 1-hour incubation. Scale bar is 12 μm. (b) Advanced period of co-localization of Met-CDs (2.5 mM, Ex = 405 nm) and mitochondria (visualized by 0.1 μM Mitotracker, Ex = 561 nm) after 24 h incubation. Yellow arrows point out the mitochondria and Met-CDs co-localizations. Scale bars are 12 μm for part (a) and 9 μm for part (b). Excitation wavelengths: Green, 405 nm, Red, 561 nm. Emission ranges: Green, 480–520 nm, Red, 579–619 nm. (For interpretation of the references to color in this figure legend, the reader is referred to the web version of this article.)

to detect Met-CDs and DAPI nucleus staining, respectively. It was revealed that Met-CDs exhibited even distribution throughout all cell structure including nucleus. When merged green and blue channels were studied, a fully matching green (Met-CDs) and blue (nucleus) patterns were observed (Fig. 6). This result supported our hypothesis about nucleus penetration of Met-CDs. Additionally, green fluorescence was not observed for the control group images of 5 min treatments (S8). As a result of two imaging studies of Met-CDs, it can be concluded that Met-CDs can dispersed throughout the whole cell structure but after approximately 1 h they start to localize inside the mitochondria of SJGBM2 tumor cells.

3.4. Crossing the Blood-Brain barrier (BBB)

Met-CDs were further investigated for their capability to penetrate the BBB. It is significant to study this ability because if the Met-CDs could effectively cross the BBB and enter the central nervous system (CNS), they could be used as a biomarker in brain tumor identification and also in fluorescence-guided brain surgery. The blood–brain barrier is one of the biggest challenges for drug delivery targeting the CNS [26]. This protection mechanism of the brain prohibits penetration of more than 90% of small molecules while almost penetration of 100% of large molecules [67]. Moreover, there are two possible pathways for molecules to cross the BBB. These pathways are passive diffusion and active transports such as receptor-, adsorption-mediated endocytosis and carrier-mediated transport [68]. A molecule must have a small size to cross the BBB via passive diffusion. On the other hand, for active routes, either specific receptors, carriers or adsorptive transcytosis sites must be involved in penetration mechanism [65]. In this study, zebrafish model was chosen due to its translucent body, rapid reproduction, easy maintenance, and genetic homology to

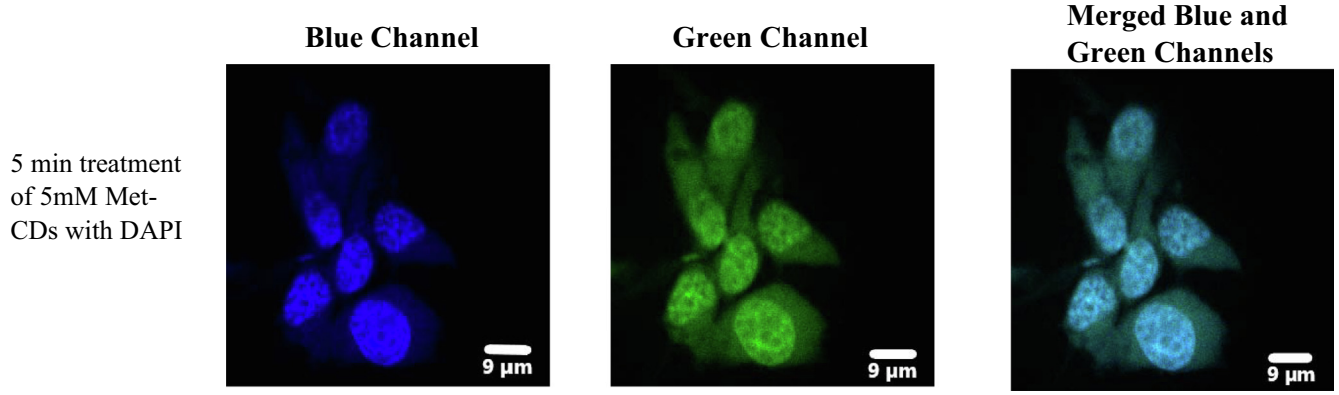

Fig. 6. Short time cell (SJGBM2) distribution of Met-CDs after 5 min of treatment imaging with confocal microscope and nucleus staining. Scale bars are 9 μm. Excitation wavelengths, green, 405 nm, blue 405 nm. Emission ranges: Green, 480–520 nm, Blue, 441–481 nm. (For interpretation of the references to color in this figure legend, the reader is referred to the web version of this article.)

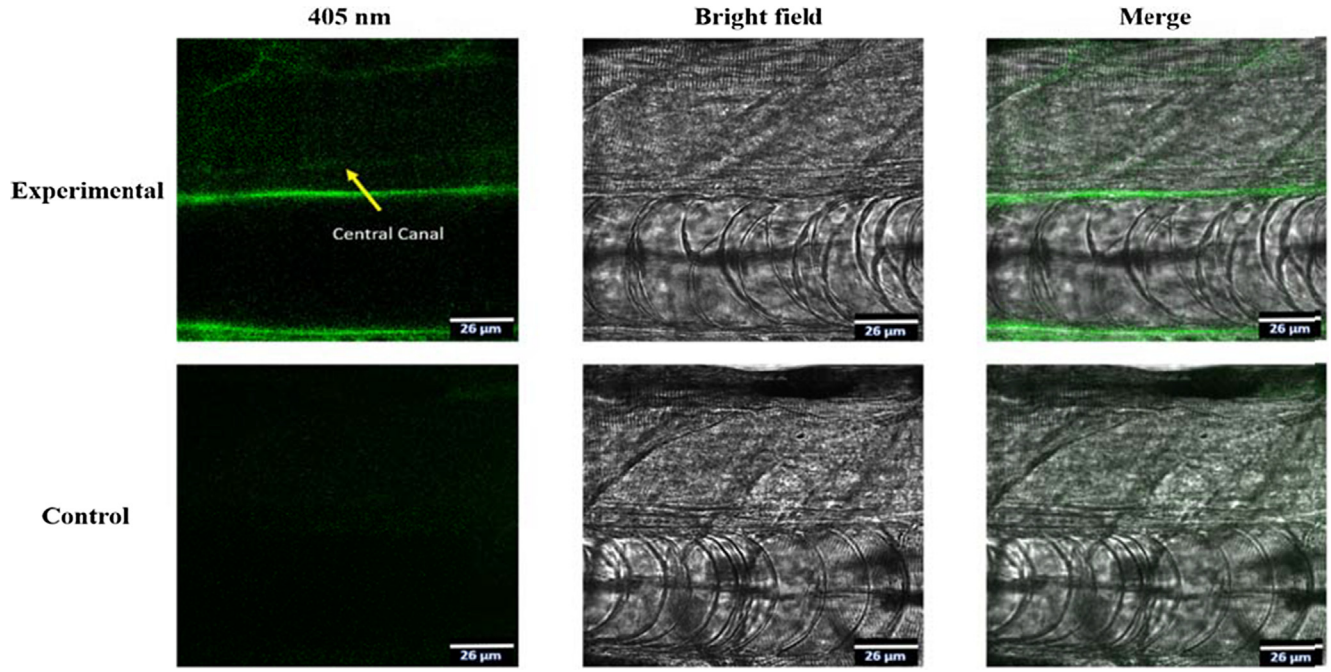

Fig. 7. Confocal microscopy images of five days post fertilization wild-type zebrafish larvae injected with 2 mg ml^{-1} of Met-CDs aqueous dispersion (top row) and the lower row represents images of a fish without any injections as the control. At the excitation of 405 nm, Fluorescence from Met-CDs which cross the BBB can be seen in the central canal (pointed with yellow arrow). Scale bars are 26 μm. (For interpretation of the references to color in this figure legend, the reader is referred to the web version of this article.)

humans [69]. The cerebral spinal fluid connects the CNS of zebrafish. The cerebral spinal fluid circulates through ventricles of the brain which is in contact with the central canal of spinal cord [26]. Any fluorescent particles which can cross the BBB can be observed in the spinal cord's central canal. For that reason, to test the ability of Met-CDs to penetrate the BBB, we observed the central canal of spinal cord to see if Met-CDs can attain in it after intravascular heart injection.

A 2 mg mL^{-1} amount of Met-CDs in aqueous dispersion was intravascularly injected into the heart of (5 days post fertilization) wild-type zebrafish. These injections were repeated with 12 zebrafish to confirm the reproducibility of the results. Then, images of treated zebrafish were taken under the excitation of 405 nm. Fig. 7 shows that at the location of the central canal of spinal cord, green PL of Met-CDs was observed. As a result, this experiment points out that Met-CDs can cross the BBB without the need of any other nanocarriers. Thus, Met-CDs also provide a potential for CNS-targeting drug delivery platform. As the possible biological pathway of Met-CDs BBB penetration, there were two explanations, passive diffusion, or carrier-mediated transport by using glutamine Na-dependent carriers. Both explanations were possible because Met-CDs possess a small size and a slightly positive charge for passive diffusion and similar structure as glutamine to use Na-dependent carriers. More specifically, the Na- dependent carriers are capable of taking up the glutamine from the brain extracellular fluid into endothelial cells [70]. We hypothesize that since the Met-CDs displayed an active cell penetration route as glutamine instead of passive diffusion in the cell lines, the same tendency might be observed for BBB penetration. In other words, Met-CDs may prefer Na-dependent glutamine carriers to cross the BBB over passive diffusion due to highly structural resemblance between Met-CDs and glutamine.

4. Conclusion

In this study, for the first time, metformin was used as one of the precursors to synthesize CDs. Met-CDs were meticulously characterized after careful purification steps. Not only was the formation of Met-CDsconfirmed, but also characteristics of Met-CDs were determined by using various characterization techniques such as UV–vis, PL, FTIR, XPS, AFM, TEM, and zeta potential. Then, cytotoxicity studies of the prepared Met-CDs were performed by using two different models, non-tumor, and tumor cell lines. From the cytotoxicity experiments, Met-CDs displayed low toxicity and good biocompatibility towards both non-tumor and tumor cells. Moreover, thanks to low toxicity, excellent biocompatibility and good PL properties, Met-CDs were further studied for bioimaging experiments as biomarkers. Initial imaging studies were executed using HEK-293 (non-cancer embryonic human kidney), DRG (non-cancer) neuronal and SJGBM2 (High-grade glioblastoma) cell lines to study Met-CDs' cell distribution and uptake in non-tumor and cancer cells. Cell distribution and uptake of Met-CDs in SJGBM2 (High-grade glioblastoma) cells were higher than HEK-293 (non-cancer embryonic human kidney) cells and DRG (non-cancer) neurons indicating selective cancer cell penetration. We related this result to highly structural resemblance between Met-CDs and glutamine. Furthermore, it was observed that Met-CDs tend to localize in a specific area of SJGBM2 (High-grade glioblastoma) cells. For this reason, organelle staining studies were conducted by using Mitotracker and DAPI nucleus staining agents. It was concluded that Met-CDs initially disperse throughout all cell structure even nucleus. But after approximately 1 h they start to localize inside the mitochondria of the SJGBM2 (High-grade glioblastoma) cells. A zebrafish study was designed to test BBB penetration properties of Met-CDs. It was demonstrated that Met-CDs cross the BBB without the need of any other ligands on their surface. Several previous studies have offered synthesis of CDs with mitochondrial targeting property [20–24]. However, this study also exhibits BBB penetration property along with mitochondrial and nucleus targeting ability of Met-CDs. Met-CDs are not only nanocarriers with surface tunable features, but also therapeutic effect enhancers. In other words, they possess abundant available functional groups on their surface for further conjugations with various therapeutics, and they improve therapeutic effects.

From this point, Met-CDs are promising drug delivery vehicles for future applications including diagnosis and treatment trials of brain related diseases, such as brain tumors, Parkinson's, and Alzheimer's diseases.

Declaration of Competing Interest

The authors declare that they have no known competing financial interests or personal relationships that could have appeared to influence the work reported in this paper.

Acknowledgements

R. M. L. thanks the support from National Science Foundation under the grant 1809060 and 2041413. Also, authors gratefully acknowledge the great support from University of Miami, USA. R. G. gratefully acknowledges the support of the Mystic Force Foundation.

Appendix A. Supplementary material

Supplementary data to this article can be found online at https://doi.org/10.1016/j.jcis.2021.02.058.

References

[1] Xin Ting Zheng, Arundithi Ananthanarayanan, Kathy Qian Luo, Peng Chen, Glowing graphene quantum dots and carbon dots: properties, syntheses, and biological applications, Small (Weinheim an der Bergstrasse, Germany). 11 (14) (2015) 1620–1636, https://doi.org/10.1002/smll.201402648.
[2] Austin M. Derfus, Warren C.W. Chan, Sangeeta N. Bhatia, Probing the cytotoxicity of semiconductor quantum dots, Nano Lett. 4 (1) (2004) 11–18, https://doi.org/10.1021/nl0347334.
[3] Esteves da Silva, C.G. Joaquim, Helena M.R. Gonçalves, Analytical and bioanalytical applications of carbon dots. TrAC, Trends Anal. Chem. 30 (8) (2011) 1327–1336, https://doi.org/10.1016/j.trac.2011.04.009.
[4] Fanglong Yuan, Shuhua Li, Zetan Fan, Xiangyue Meng, Louzhen Fan, Shihe Yang, Shining carbon dots: synthesis and biomedical and optoelectronic applications, Nano Today 11 (5) (2016) 565–586, https://doi.org/10.1016/j.nantod.2016.08.006.
[5] Changqin Ding, Anwei Zhu, Yang Tian, Functional surface engineering of c-dots for fluorescent biosensing and in vivo bioimaging, Acc. Chem. Res. 47 (1) (2014) 20–30, https://doi.org/10.1021/ar400023s.
[6] K.A. Shiral Fernando, Sushant Sahu, Yamin Liu, et al., Carbon quantum dots and applications in photocatalytic energy conversion, ACS Appl. Mater. Interfaces 2015; 7(16): 8363–8376. doi: 10.1021/acsami.5b00448.
[7] Vaibhavkumar N. Mehta, Sanjay Jha, Hirakendu Basu, Rakesh Kumar Singhal, Suresh Kumar Kailasa, One-step hydrothermal approach to fabricate carbon dots from apple juice for imaging of mycobacterium and fungal cells, Sens. Actuators B Chem. 213 (2015) 434–443, https://doi.org/10.1016/j.snb.2015.02.104.
[8] Sajini D. Hettiarachchi, Regina M. Graham, Keenan J. Mintz, et al., Triple conjugated carbon dots as a nano-drug delivery model for glioblastoma brain tumors, Nanoscale 11 (13) (2019) 6192–6205, https://doi.org/10.1039/c8nr08970a.
[9] Pengli Gao, Shi Liu, Ya Su, Min Zheng, Zhigang Xie, Fluorine-doped carbon dots with intrinsic nucleus-targeting ability for drug and dye delivery, Bioconjug. Chem. 31 (3) (2020) 646–655, https://doi.org/10.1021/acs.bioconjchem.9b00801.
[10] R.S. Hundal, S.E. Inzucchi, Metformin: new understandings, new uses, Drugs. 63 (18) (2003) 1879–1894, https://doi.org/10.2165/00003495-200363180-00001.
[11] L.A. Witters, The blooming of the french lilac, J. Clin. Investig. 108 (8) (2001) 1105–1107, https://doi.org/10.1172/JCI14178.
[12] Garry G. Graham, Jeroen Punt, Manit Arora, et al., Clinical pharmacokinetics of metformin, Clin. Pharmacokinet. 50 (2) (2011) 81–98, https://doi.org/10.2165/11534750-000000000-00000.
[13] Graham Rena, D. Grahame Hardie, Ewan R. Pearson, The mechanisms of action of metformin, Diabetologia 60 (9) (2017) 1577–1585, https://doi.org/10.1007/s00125-017-4342-z.
[14] Magdalena Markowicz-Piasecka, Ibrahim Komeil, Johanna Huttunen, Joanna Sikora, Kristiina M. Huttunen, Effective cellular transport of ortho - halogenated sulfonamide derivatives of metformin is related to improved antiproliferative activity and apoptosis induction in mcf-7 cells, Int. J. Mol. Sci. 21 (7) (2020) 2389–2418, https://doi.org/10.3390/ijms21072389.
[15] Clifford J. Bailey, Robert C. Metformin Turner, New England J. Med. 1996; 334 (9): 574–579. doi: 10.1056/nejm199602293340906.
[16] Fuyuko Takata, Shinya Dohgu, Junichi Matsumoto, et al., Metformin induces up-regulation of blood–brain barrier functions by activating amp-activated protein kinase in rat brain microvascular endothelial cells, Biochem. Biophys. Res. Commun. 433 (4) (2013) 586–590, https://doi.org/10.1016/j.bbrc.2013.03.036.
[17] Ryan J.O. Dowling, Saroj Niraula, Vuk Stambolic, Pamela J. Goodwin, Metformin in cancer: translational challenges, J. Mol. Endocrinol. 48 (3) (2012) R31–R43, https://doi.org/10.1530/jme-12-0007.
[18] Chad P. Satori, Michelle M. Henderson, Elyse A. Krautkramer, Vratislav Kostal, Mark M. Distefano, Edgar A. Arriaga, Bioanalysis of eukaryotic organelles, Chem. Rev. 113 (4) (2013) 2733–2811, https://doi.org/10.1021/cr300354g.
[19] Dmitri B. Papkovsky, Ruslan I. Dmitriev, Biological detection by optical oxygen sensing, Chem. Soc. Rev. 42 (22) (2013) 8700–8732, https://doi.org/10.1039/c3cs60131e.
[20] Xian-Wu Hua, Yan-Wen Bao, Zhan Chen, Fu-Gen Wu, Carbon quantum dots with intrinsic mitochondrial targeting ability for mitochondria-based theranostics, Nanoscale. 9 (30) (2017) 10948–10960, https://doi.org/10.1039/c7nr03658b.
[21] M. Karbowski, R.J. Youle, Dynamics of mitochondrial morphology in healthy cells and during apoptosis, Cell Death Differ. 10 (8) (2003) 870–880, https://doi.org/10.1038/sj.cdd.4401260.
[22] Brenno A.D. Neto, José R. Corrêa, Rafael G. Silva, Selective mitochondrial staining with small fluorescent probes: importance, design, synthesis, challenges and trends for new markers, RSC Adv. 3 (16) (2013) 5291–5301, https://doi.org/10.1039/c2ra21995f.
[23] Ye Zhang, Yajing Shen, Xiyao Teng, Manqing Yan, Hong Bi, Paulo Cesar Morais, Mitochondria-targeting nanoplatform with fluorescent carbon dots for long time imaging and magnetic field-enhanced cellular uptake, ACS Appl. Mater. Interfaces 7 (19) (2015) 10201–10212, https://doi.org/10.1021/acsami.5b00405.
[24] Xin Geng, Yuanqiang Sun, Zhaohui Li, et al., Retrosynthesis of tunable fluorescent carbon dots for precise long-term mitochondrial tracking, Small (Weinheim an der Bergstrasse, Germany) 15(48) (2019) 1901517-n/a. doi: 10.1002/smll.201901517.
[25] Shiyao Zhou, Qi Shang, Ningning Wang, Qian Li, Aixin Song, Yuxia Luan, Rational design of a minimalist nanoplatform to maximize immunotherapeutic efficacy: Four birds with one stone, J. Control. Release 328 (2020) 617–630, https://doi.org/10.1016/j.jconrel.2020.09.035.
[26] Yiqun Zhou, Zhili Peng, Elif S Seven, Roger M. Leblanc, Crossing the blood-brain barrier with nanoparticles, J. Control. Release 270 (2018) 290–303, https://doi.org/10.1016/j.jconrel.2017.12.015.
[27] Shousi Lu, Shanshan Guo, Pingxiang Xu, et al., Hydrothermal synthesis of nitrogen-doped carbon dots with real-time live-cell imaging and blood-brain barrier penetration capabilities, Int. J. Nanomed. 11 (2016) 6325–6336, https://doi.org/10.2147/IJN.S119252.
[28] Cinzia M. Bellettato, Maurizio Scarpa. Possible strategies to cross the blood–brain barrier, Italian J. Pediatr. 44(S2) (2018) 131–131. doi: 10.1186/s13052-018-0563-0.
[29] Q. Cai, L. Wang, G. Deng, J. Liu, Q. Chen, Z. Chen, Systemic delivery to central nervous system by engineered PLGA nanoparticles, Am. J. Transl. Res. 8 (2) (2016) 749–764.
[30] Krzysztof Łabuzek, Dariusz Suchy, Bożena Gabryel, Anna Bielecka, Sebastian Liber, Bogusław Okopień, Quantification of metformin by the hplc method in brain regions, cerebrospinal fluid and plasma of rats treated with lipopolysaccharide, Pharmacol. Rep. 62 (5) (2010) 956–965, https://doi.org/10.1016/s1734-1140(10)70357-1.
[31] Yanqun Liu, Guanghui Tang, Yaning Li, et al., Metformin attenuates blood-brain barrier disruption in mice following middle cerebral artery occlusion, J. Neuroinflamm. 11(1) (2014) 177–177. doi: 10.1186/s12974-014-0177-4.
[32] Yiwen Ji, Yiqun Zhou, Eric Waidely, et al., Rheology of a carbon dot gel, Inorg. Chim. Acta 468 (2017) 119–124, https://doi.org/10.1016/j.ica.2017.07.046.
[33] Yiqun Zhou, Piumi Y. Liyanage, Daniel L. Geleroff, et al., Photoluminescent carbon dots: a mixture of heterogeneous fractions, ChemPhysChem 19 (19) (2018) 2589–2597, https://doi.org/10.1002/cphc.201800248.
[34] Elif S. Seven, Shiv K. Sharma, Dihya Meziane, et al., Close-packed Langmuir monolayers of saccharide-based carbon dots at the air–subphase interface, Langmuir 35 (20) (2019) 6708–6718, https://doi.org/10.1021/acs.langmuir.9b00920.
[35] Keenan J Mintz, Guillaume Mercado, Yiqun Zhou, et al., Tryptophan carbon dots and their ability to cross the blood-brain barrier, Colloids Surf., B 176 (2019) 488–493, https://doi.org/10.1016/j.colsurfb.2019.01.031.
[36] C.D. Wagner, L.E. Davis, M.V. Zeller, J.A. Taylor, R.H. Raymond, L.H. Gale, Empirical atomic sensitivity factors for quantitative analysis by electron spectroscopy for chemical analysis, Surf. Interface Anal. 3 (5) (1981) 211–225, https://doi.org/10.1002/sia.740030506.
[37] D.A. Shirley, High-resolution x-ray photoemission spectrum of the valence bands of gold, Phys. Rev. B, Solid State 5 (12) (1972) 4709–4714, https://doi.org/10.1103/physrevb.5.4709.
[38] Donald W. Moore, James A. Happe, The proton magnetic resonance spectra of some metal vinyl compounds, J. Phys. Chem. 1961; 65(2) (1952) 224–229. doi:10.1021/j100820a008
[39] A. Pardo, D. Reyman, J.M.L. Poyato, F. Medina, Some β-carboline derivatives as fluorescence standards, J. Lumin. 51 (5) (1992) 269–274, https://doi.org/10.1016/0022-2313(92)90077-M.
[40] James N. Sleigh, Greg A. Weir, Giampietro Schiavo, A simple, step-by-step dissection protocol for the rapid isolation of mouse dorsal root ganglia, BMC Res. Notes 9(1) (2016) 82-82. doi: 10.1186/s13104-016-1915-8.

[41] Tayline V. De Medeiros, John Manioudakis, Farah Noun, Jun-Ray Macairan, Florence Victoria, Rafik Naccache, Microwave-assisted synthesis of carbon dots and their applications, J. Mater. Chem. C, Mater. Opt. Electronic Dev. 7(24) (2019) 7175–7195. 10.1039/c9tc01640f.
[42] Piumi Y. Liyanage, Regina M. Graham, Raja R. Pandey, et al., Carbon nitride dots: a selective bioimaging nanomaterial, Bioconjug. Chem. 30 (1) (2019) 111–123, https://doi.org/10.1021/acs.bioconjchem.8b00784.
[43] Sen Liu, Jingqi Tian, Lei Wang, Yonglan Luo, Xuping Sun, A general strategy for the production of photoluminescent carbon nitride dots from organic amines and their application as novel peroxidase-like catalysts for colorimetric detection of H_2O_2 and glucose, RSC Adv. 2 (2) (2012) 411–413, https://doi.org/10.1039/C1RA00709B.
[44] Bart Van Dam, Hui Nie, Bo Ju, et al., Carbon Dots: Excitation-dependent photoluminescence from single-carbon dots (Small 48/2017), Small (Weinheim an der Bergstrasse, Germany) 13(48) (2017) 1770251-n/a. doi:10.1002/smll.201770251
[45] K. Mintz, Y. Zhou, R. Leblanc, Recent development of carbon quantum dots regarding their optical properties, photoluminescence mechanism, and core structure, Nanoscale. 11 (11) (2019) 4634–4652.
[46] Shoujun Zhu, Qingnan Meng, Lei Wang, et al., Highly photoluminescent carbon dots for multicolor patterning, sensors, and bioimaging, Angewandte Chemie (International ed) 52 (14) (2013) 3953–3957, https://doi.org/10.1002/anie.201300519.
[47] Hui Ding, Ji-Shi Wei, Ning Zhong, Qing-Yu Gao, Huan-Ming Xiong, Highly efficient red-emitting carbon dots with gram-scale yield for bioimaging, Langmuir 33 (44) (2017) 12635–12642, https://doi.org/10.1021/acs.langmuir.7b02385.
[48] Junqing Wang, Pengfei Zhang, Chao Huang, Gang Liu, Ken Cham-Fai Leung, Yì Xiáng J. Wáng, High performance photoluminescent carbon dots for in vitro and in vivo bioimaging: effect of nitrogen doping ratios. Langmuir 31(29) (2015) 8063–8073. doi:10.1021/acs.langmuir.5b01875
[49] Prasad V. Bharatam, Rajnish Moudgil, Damanjit Kaur, Electron delocalization in isocyanates, formamides, and ureas: importance of orbital interactions, J. Phys. Chem. A Mol., Spectrosc., Kinet., Environ., General Theory. 107 (10) (2003) 1627–1634, https://doi.org/10.1021/jp027044+.
[50] Yiqun Zhou, Elsayed M Zahran, Bruno A Quiroga, et al., Size-dependent photocatalytic activity of carbon dots with surface-state determined photoluminescence, Appl. Catal. B, Environ.. 248 (2019) 157–166, https://doi.org/10.1016/j.apcatb.2019.02.019.
[51] Ting Ho Lee, J. Wayne Rabalais, X-ray photoelectron spectra and electronic structure of some diamine compounds, J. Electron Spectrosc. Relat. Phenom. 11 (1) (1977) 123–127, https://doi.org/10.1016/0368-2048(77)85052-4.
[52] Hameed Shah, Qi Xin, Xinrui Jia, Jian Ru Gong, Single precursor-based luminescent nitrogen-doped carbon dots and their application for iron (III) sensing, Arabian J. Chem. 12 (7) (2019) 1083–1091, https://doi.org/10.1016/j.arabjc.2019.06.004.
[53] S. Mourdikoudis, R. Pallares, N. Thanh, Characterization techniques for nanoparticles: comparison and complementarity upon studying nanoparticle properties, Nanoscale. 10 (27) (2018) 12871–12934, https://doi.org/10.1039/c8nr02278j.
[54] David N. Hendrickson, Jack M. Hollander, William L. Jolly, Nitrogen ls electron binding energies. Correlations with molecular orbital calculated nitrogen charges, Inorg. Chem. 8 (12) (1969) 2642–2647, https://doi.org/10.1021/ic50082a020.
[55] Qin Li, Tymish Y. Ohulchanskyy, Ruili Liu, et al., Photoluminescent carbon dots as biocompatible nanoprobes for targeting cancer cells in vitro, J. Phys. Chem. C 114 (28) (2010) 12062–12068, https://doi.org/10.1021/jp911539r.
[56] Bhaskar Garg, Tanuja Bisht, Yong-Chien Ling, Graphene-based nanomaterials as heterogeneous acid aatalysts: a comprehensive perspective, Molecules (Basel, Switzerland). 19 (9) (2014) 14582–14614, https://doi.org/10.3390/molecules190914582.
[57] Kofi Oti Boakye-Yiadom, Samuel Kesse, Yaw Opoku-Damoah, et al., Carbon dots: Applications in bioimaging and theranostics, Int. J. Pharm. 564 (2019) 308–317, https://doi.org/10.1016/j.ijpharm.2019.04.055.
[58] Paul L. McNeil, Richard A. Steinhardt, Plasma membrane disruption: repair, prevention, adaptation, Ann. Rev. Cell Develop. Biol. 19 (1) (2003) 697–731, https://doi.org/10.1146/annurev.cellbio.19.111301.140101.
[59] A.N. Emam, Samah A. Loutfy, Amany A. Mostafa, H. Awad, Mona B. Mohamed, Cyto-toxicity, biocompatibility and cellular response of carbon dots–plasmonic based nano-hybrids for bioimaging, RSC Adv. 7 (38) (2017) 23502–23514, https://doi.org/10.1039/c7ra01423f.
[60] Julie Sesen, Perrine Dahan, Sarah J. Scotland, et al., Metformin inhibits growth of human glioblastoma cells and enhances therapeutic response. PloS one 10 (4) (2015) e0123721-e0123721. doi:10.1371/journal.pone.0123721
[61] Roberto Würth, Alessandra Pattarozzi, Monica Gatti, et al., Metformin selectively affects human glioblastoma tumor-initiating cell viability, Cell cycle (Georgetown, Tex) 12 (1) (2013) 145–156, https://doi.org/10.4161/cc.23050.
[62] Seung Ho Yang, Shenglan Li, Guangrong Lu, et al., Metformin treatment reduces temozolomide resistance of glioblastoma cells, Oncotarget. 7 (48) (2016) 78787–78803, https://doi.org/10.18632/oncotarget.12859.
[63] M. Monici, Cell and tissue autofluorescence research and diagnostic applications, Biotechnol. Annu. Rev. 11 (2005) 227–256, https://doi.org/10.1016/S1387-2656(05)11007-2.
[64] Siva Kumar Natarajan, Sriram Venneti, Glutamine metabolism in brain tumors, Cancers 11(11) (2019) 1628–1628. doi:10.3390/cancers11111628
[65] Jhudit Pérez-Escuredo, Rajesh K. Dadhich, Suveera Dhup, et al., Lactate promotes glutamine uptake and metabolism in oxidative cancer cells, Cell cycle (Georgetown, Tex) 15 (1) (2016) 72–83, https://doi.org/10.1080/15384101.2015.1120930.
[66] Sylvia Andrzejewski, Simon-Pierre Gravel, Michael Pollak, Julie St-Pierre, Metformin directly acts on mitochondria to alter cellular bioenergetics, Cancer Metabolism. 2 (1) (2014) 12–26, https://doi.org/10.1186/2049-3002-2-12.
[67] Richard Daneman, Alexandre Prat, The blood–brain barrier, Cold Spring Harbor Perspect. Biol. 7 (1) (2015) a020412–a20426, https://doi.org/10.1101/cshperspect.a020412.
[68] Jaleh Barar, Mohammad A. Rafi, Mohammad M. Pourseif, Yadollah Omidi, Blood-brain barrier transport machineries and targeted therapy of brain diseases, Bioimpacts. 6 (4) (2016) 225–248, https://doi.org/10.15171/bi.2016.30.
[69] Ye Li, Tongkai Chen, Xiaoqing Miao, et al., Zebrafish: A promising in vivo model for assessing the delivery of natural products, fluorescence dyes and drugs across the blood-brain barrier, Pharmacol. Res. 125(Pt B) (2017) 246–257. doi:10.1016/j.phrs.2017.08.017
[70] Wha-Joon Lee, Richard A. Hawkins, Juan R. Viña, Darryl R. Peterson, Glutamine transport by the blood-brain barrier: a possible mechanism for nitrogen removal, Am. J. Physiol.: Cell Physiol. 274 (4) (1998) C1101–C1107, https://doi.org/10.1152/ajpcell.1998.274.4.c1101.